Numerical modeling of the emplacement of Socompa rock avalanche, Chile

K. Kelfoun and T. H. Druitt
Laboratoire Magmas et Volcans, OPGC, UBP–CNRS–IRD, Clermont-Ferrand, France

Received 1 April 2005; revised 27 June 2005; accepted 14 September 2005; published 16 December 2005.

[1] The 7.5 ka Socompa sector collapse emplaced 25 km^3 of fragmented rock as a thin, but widespread (500 km^2), avalanche deposit, followed by late stage sliding of 11 km^3 as Toreva blocks. Most of the avalanche mass was emplaced dry, although saturation of a basal shear layer cannot be excluded. Modeling was carried out using the depth-averaged granular flow equations in order to provide information on the flow behavior of this well-preserved, long run-out avalanche. Results were constrained using structures preserved on the surface of the deposit, as well as by deposit outline and run-up (a proxy for velocity). Models assuming constant dynamic friction fail to produce realistic results because the low basal friction angles (1 to 3.5°) necessary to generate observed run-out permit neither adequate deposition on slopes nor preservation of significant morphology on the deposit surface. A reasonable fit is obtained, however, if the avalanche is assumed simply to experience a constant retarding stress of 50–100 kPa during flow. This permits long run-out as well as deposition on slopes and preservation of realistic depositional morphology. In particular the model explains a prominent topographic escarpment on the deposit surface as the frozen front of a huge wave of debris reflected off surrounding hills. The result that Socompa avalanche experienced a small, approximately constant retarding stress during emplacement is consistent with a previously published analysis of avalanche data.

Citation: Kelfoun, K., and T. H. Druitt (2005), Numerical modeling of the emplacement of Socompa rock avalanche, Chile, *J. Geophys. Res.*, *110*, B12202, doi:10.1029/2005JB003758.

1. Introduction

[2] Long run-out rock or debris avalanches are one of the most hazardous of geological phenomena [*Melosh*, 1990]. During emplacement, the center of mass follows a low-angle ($\ll 30°$) trajectory, forming a thin, widespread deposit. Avalanches on Earth with volumes greater than 10^6 m^3 are generally of long run-out type. Long run-out avalanches are emplaced in a catastrophic manner, with observed or inferred velocities of 20–100 m s^{-1} and run-outs reaching in some cases many tens of km. They occur both in terrestrial and marine environments by sudden mobilization of large rock masses, either in volcanic or nonvolcanic contexts. The ability of avalanches to travel large distances in a fluid-like manner is not well understood, apparently requiring greatly reduced dynamic friction, and a number of possible friction reduction mechanisms have been proposed (see recent articles by *Davies and McSaveney* [1999], *Legros* [2002], and *Collins and Melosh* [2003] and references therein).

[3] In this paper we use numerical modeling to place constraints on the flow dynamics of the long run-out avalanche that formed 7500 years ago by sector collapse of Socompa Volcano in northern Chile. The model solves the equations of motion for a granular flow and has the advantage of taking into account basal friction, internal friction and volumetric spreading behavior in a rigorous manner. The modeling is constrained by deposit outline, run-up (a proxy for velocity), and structures preserved on the surface of the deposit when the avalanche ceased motion. In particular we seek to explain the formation of high topographic escarpment that is a prominent feature of the avalanche deposit. The study provides some crude, but intriguing, constraints on the rheological behavior of the avalanche during motion.

2. Socompa Avalanche

[4] Socompa avalanche in northern Chile (Figure 1) has been described in papers by *Francis et al.* [1985], *Wadge et al.* [1995], and *Van wyk de Vries et al.* [2001], on which the following summary is based. It formed by gravitational collapse of the northwestern flank of the 6000-m-high stratovolcano, leaving an amphitheater 12 km wide at its mouth and with cliffs 300–400 m high. The avalanche flowed across a broad topographic basin northwest of the volcano (Monturaqui Basin) to a maximum distance of 40 km, and covered 500 km^2. The vertical drop from the volcano summit to the lowest point of the basin was 3000 m; at its northwestern limit the avalanche rode part way up a range of hills before being deflected to the

0148-0227/05/2005JB003758$09.00

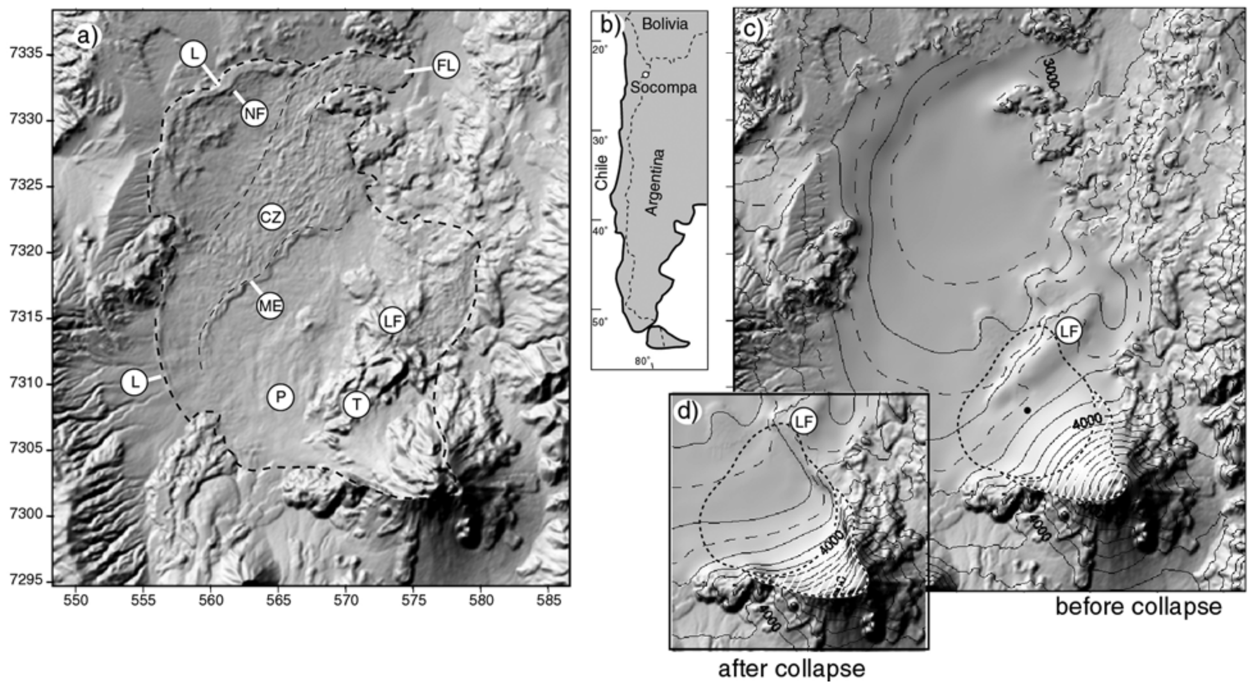

Figure 1. (a) Shaded topography of Socompa avalanche, showing the median escarpment (ME), the frontal lobe (FL), thick distal levees (L) cut by large normal faults (NF), and the central morphologically rough zone (CZ). The accumulation of Toreva blocks is marked (T). La Flexura (LF) is a basement anticline predating sector collapse. Deposits from later pyroclastic flows are marked (P). Coordinates are given in km (UTM, WGS84). (b) Location of Socompa Volcano in northern Chile. Reconstructed topography (c) of the area before collapse and (d) of the failure surface. The 25 km^3 that collapsed to form the avalanche in the "deep" collapse model is outlined by a black dotted line; the white ruled area is the 11 km^3 that slumped after collapse and which was left in place in our calculations. The contact between the two volumes is taken as a hemi-cylindrical headwall scarp 5 km in radius. In the "shallow" collapse model the 25 km^3 that collapsed is taken as a slab representing the upper 69.4% (=25/36) of the entire 36 km^3 area.

northeast, forming a frontal lobe. The volume of rock transported is estimated to be about 25 km^3, with another 11 km^3 preserved as intact ("Toreva") blocks up to 400 m high at the foot of the collapse scarp.

[5] The morphology of the avalanche deposit is perfectly preserved in the hyperarid climate of the Atacama Desert (Figure 1a). The margins are steep and well defined, with thicknesses ranging from 10 to 60 m [*Wadge et al.*, 1995]. In some places, levees are present (labeled L on Figure 1a). A zone of convergence and SE verging thrusting called the "median escarpment" (ME on Figure 1a) separates the proximal part of the deposit, characterized by longitudinal surface ridges, from the distal part characterized by convoluted surface texture [*Van wyk de Vries et al.*, 2001]. A complex assemblage of surface structures including normal faults, strike-slip faults, thrusts, and longitudinal and transverse ridges records the last increments of movement of the avalanche on a local scale. The 5-km-wide central zone (CZ on Figure 1a) immediately north of the median escarpment is particularly rich in structures (Figure 1a) and lies 30–60 m higher than neighboring areas.

[6] Ignimbrites, gravels, sands, and minor lacustrine evaporites from the subvolcanic Salin Formation dominate the avalanche sheet (reconstituted ignimbrite facies; RIF $\sim$ 80%). Brecciated lavas and volcaniclastic deposits from the edifice itself (Socompa breccia facies; SB) constitute $\sim$20% and are confined mainly to the upper levels of the deposit. The eastern half and outer margins of the deposit consists almost entirely of RIF, with a thin overlying layer of SB no thicker than a couple of meters, whereas the southwestern half is composed of RIF overlain by up to 15 m of SB (see Figure 10e in section 5).

[7] Most of the avalanche probably formed by a series of retrogressive failures that merged to form a single moving mass [*Wadge et al.*, 1995]. Spreading took place as a semirigid mass on a basal layer of shearing RIF [*Van wyk de Vries et al.*, 2001]. The RIF behaved in a ductile fashion and must have been very weak mechanically to accommodate flow on slopes of 5° or less, as confirmed by the modeling presented below. The SB, on the other hand, behaved in a brittle fashion, breaking up passively as it rode on a layer of RIF lubricant. Perfect preservation of the avalanche margins, and the absence of distal mudflows, shows that any interstitial water was present in insufficient quantities to saturate the majority of the flowing debris.

3. Numerical Modeling of the Avalanche

3.1. Basic Equations

[8] The assumption is made in our model that the bulk of the avalanche slid on a thin basal layer. This is commonly

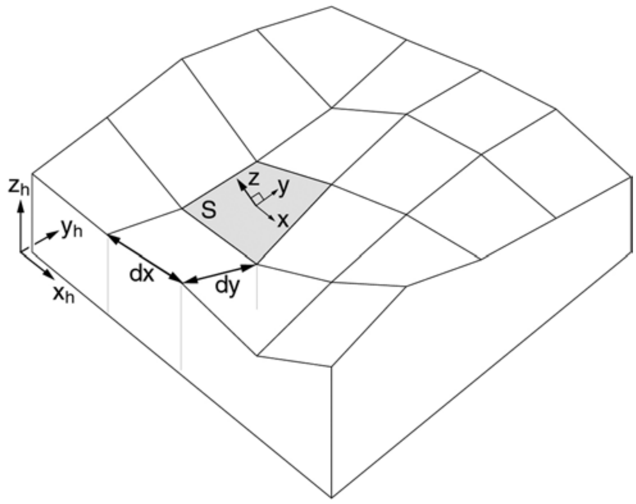

Figure 2. Geometry of the calculation domain. The ground topography is defined using horizontal axes x_h and y_h, and vertical axis z_h. The avalanche coordinates and thickness are defined using topography-linked axes x, y, and z. The cell dimensions are dx and dy.

assumed in modeling granular flows [e.g., *Savage and Hutter*, 1989, 1991; *Iverson*, 1997; *Iverson and Denlinger*, 2001; *Denlinger and Iverson*, 2001; *Heinrich et al.*, 2001; *Patra et al.*, 2005] and is consistent with field evidence at Socompa and other long run-out avalanches [*Shaller*, 1991; *Takarada et al.*, 1999; *van Wyk de Vries et al.*, 2001].

[9] Using a topography-linked coordinate system (Figure 2), with x and y parallel to the local ground surface and h perpendicular to it, the general depth-averaged equations of mass (equation (1)) and momentum (equations (2) and (3)) conservation are

$$\frac{\partial h}{dt} + \frac{\partial}{\partial x}(hu) + \frac{\partial}{\partial y}(hv) = 0 \tag{1}$$

$$\frac{\partial}{\partial t}(hu) + \frac{\partial}{\partial x}\left(hu^2\right) + \frac{\partial}{\partial y}(huv) = gh\sin\alpha_x - \frac{1}{2}k_{\mathrm{actpass}}\frac{\partial}{\partial x}\left(gh^2\cos\alpha\right) + \frac{T_x}{\rho} \tag{2}$$

$$\frac{\partial}{\partial t}(hv) + \frac{\partial}{\partial x}(hvu) + \frac{\partial}{\partial y}\left(hv^2\right) = gh\sin\alpha_y - \frac{1}{2}k_{\mathrm{actpass}}\frac{\partial}{\partial y}\left(gh^2\cos\alpha\right) + \frac{T_y}{\rho} \tag{3}$$

where h is flow thickness, $\mathbf{u} = (u, v)$ is flow velocity, α is ground slope, $\mathbf{T}$ is retarding stress, ρ is bulk density of the avalanche, k_{actpass} is Earth pressure coefficient (ratio of ground-parallel to ground-normal stress), and subscripts denote components in the x and y directions.

[10] For a dry frictional material, the retarding stress is of the form

$$T_x = -\rho h\left(g\cos\alpha + \frac{\mathbf{u}^2}{r}\right)\tan\varphi_{\mathrm{bed}}\frac{u}{\|\mathbf{u}\|} \tag{4}$$

where φ_{bed} is the angle of dynamic friction between the avalanche and the ground surface and any excess pore fluid pressure is assumed to be negligible. Use of this law, even in cases of rapid granular flow, is justified by *Savage and Hutter* [1989]. Shear cell tests show that the ratio of shear to normal stresses in a rapidly deforming granular material can be represented by an approximately constant dynamic friction coefficient, even if interparticle collisions are important. The second term in parentheses is the centrifugal stress, where r is the radius of curvature of the ground [*Savage and Hutter*, 1991]. The y component of $\mathbf{T}$ is obtained by replacing u by v.

[11] Following *Iverson and Denlinger* [2001], the expression for k_{actpass} used if the internal behavior is frictional is

$$k_{\mathrm{actpass}} = 2\,\frac{1 \pm \left[1 - \cos^2\varphi_{\mathrm{int}}\left(1 + \tan^2\varphi_{\mathrm{bed}}\right)\right]^{1/2}}{\cos^2\varphi_{\mathrm{int}}} - 1 \tag{5}$$

where φ_{int} is the internal angle of friction of the avalanche. This expression is valid if $\varphi_{\mathrm{bed}} < \varphi_{\mathrm{int}}$. The sign $\pm$ is negative (and k_{actpass} active) where the local flow is divergent and is positive (and k_{actpass} passive) where the local flow is convergent. If, on the other hand, $\varphi_{\mathrm{bed}} \geq \varphi_{\mathrm{int}}$, then k_{actpass} is given by

$$k_{\mathrm{actpass}} = \frac{1 + \sin^2\varphi_{\mathrm{int}}}{1 - \sin^2\varphi_{\mathrm{int}}} \tag{6}$$

3.2. Numerical Scheme

[12] The equations were solved numerically using a shock-capturing method based on a double upwind Eulerian scheme (Appendix A). The scheme can handle shocks, rarefaction waves, and granular jumps and is stable even on complex topography and on both numerically "wet" and "dry" surfaces. Some numerical schemes require the ground ahead of the avalanche to be covered with a very thin artificial layer of avalanche material: a so-called numerically wet surface [*Toro*, 2001].

[13] In order to check the accuracy of our numerical scheme we performed tests to compare the numerical results with analytical solutions and with simulations based on other numerical schemes. Some of these are presented here. Figures 3–5 show comparisons between numerical and exact solutions of dam break problems. In the first case (Figure 3) the slope is horizontal and there is zero friction. This problem simulates the breakage of a dam separating an initial layer 1.5 m thick (left) from a layer 0.5 m thick (right). Our solution reproduces almost exactly the analytical solution, and particularly the frontal shock wave and the thickness of the central plateau.

[14] Figure 4 shows three comparisons with exact solutions obtained by *Mangeney et al.* [2000] for a dam break problem on a slope with nonzero friction and with zero thickness in front of the initial dam. The shape and velocity of the flow are accurately reproduced, even for the least favorable case of a steep slope and high friction angle. Note that vertical expansion of the y axis exaggerates the difference between numerical and analytical solutions.

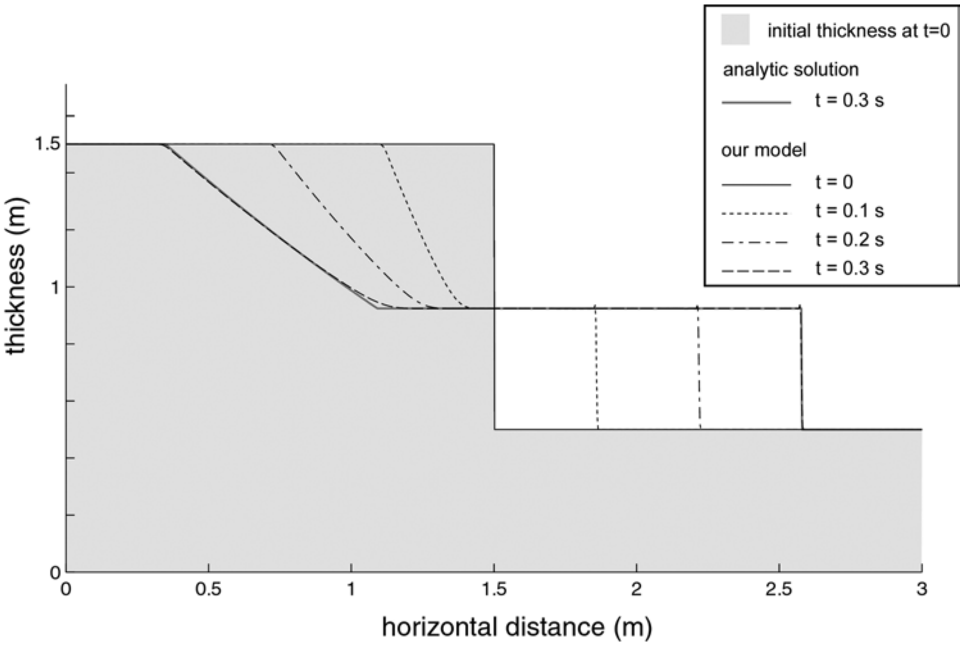

Figure 3. Comparison between numerical and analytical solutions for a dam break onto a numerically "wet" surface, in the absence of friction. An initial 1.5-m-thick layer is released onto a 0.5-m-thick layer. Points of the analytical solution for t = 0.3 s are (x = 0, h = 1.5) (0.3492, 1.5) (1.0915, 0.924289) (2.5781, 0.924289) (3 0.5). Note the good fit between the two solutions at t = 0.3 s and the accurate reproduction of the front. The thickness of the plateau obtained by our numerical solution is between 0.9240 and 0.9244, compared with 0.924289 for the analytical solution. Parameters used are dx_h = 2.5 mm, $dt = 1 \times 10^{-4}$ s, and g = 9.81 m s^{-2}.

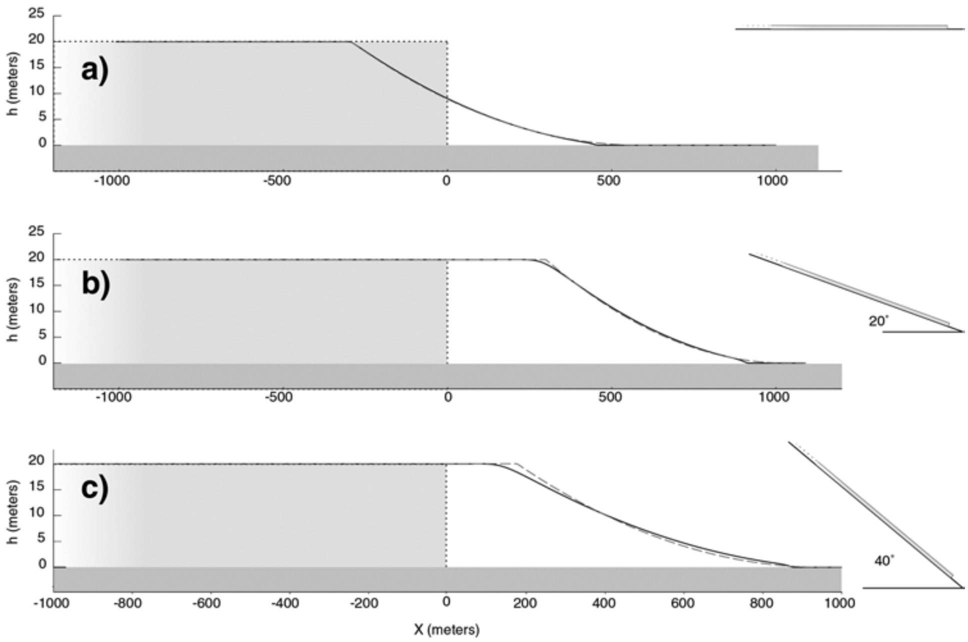

Figure 4. Comparison between the analytical solution of *Mangeney et al.* [2000] (dashed gray), and our numerical model (solid black) for a frictional dam break flow onto a numerically "dry" surface. (a) Horizontal surface (α = 0°) with no friction (φ_{bed} = 0°) at t = 21 s; (b) α = 20°, no friction (φ_{bed} = 0°) at 18 s, and (c) α = 40°, φ_{bed} = 30° at 21 s. Parameters used are dx_h = 1 m, $dt = 10^{-2}$ s, and g = 9.81 m s^{-2}. The figures to the right show the initial shape at t = 0, without vertical exaggeration.

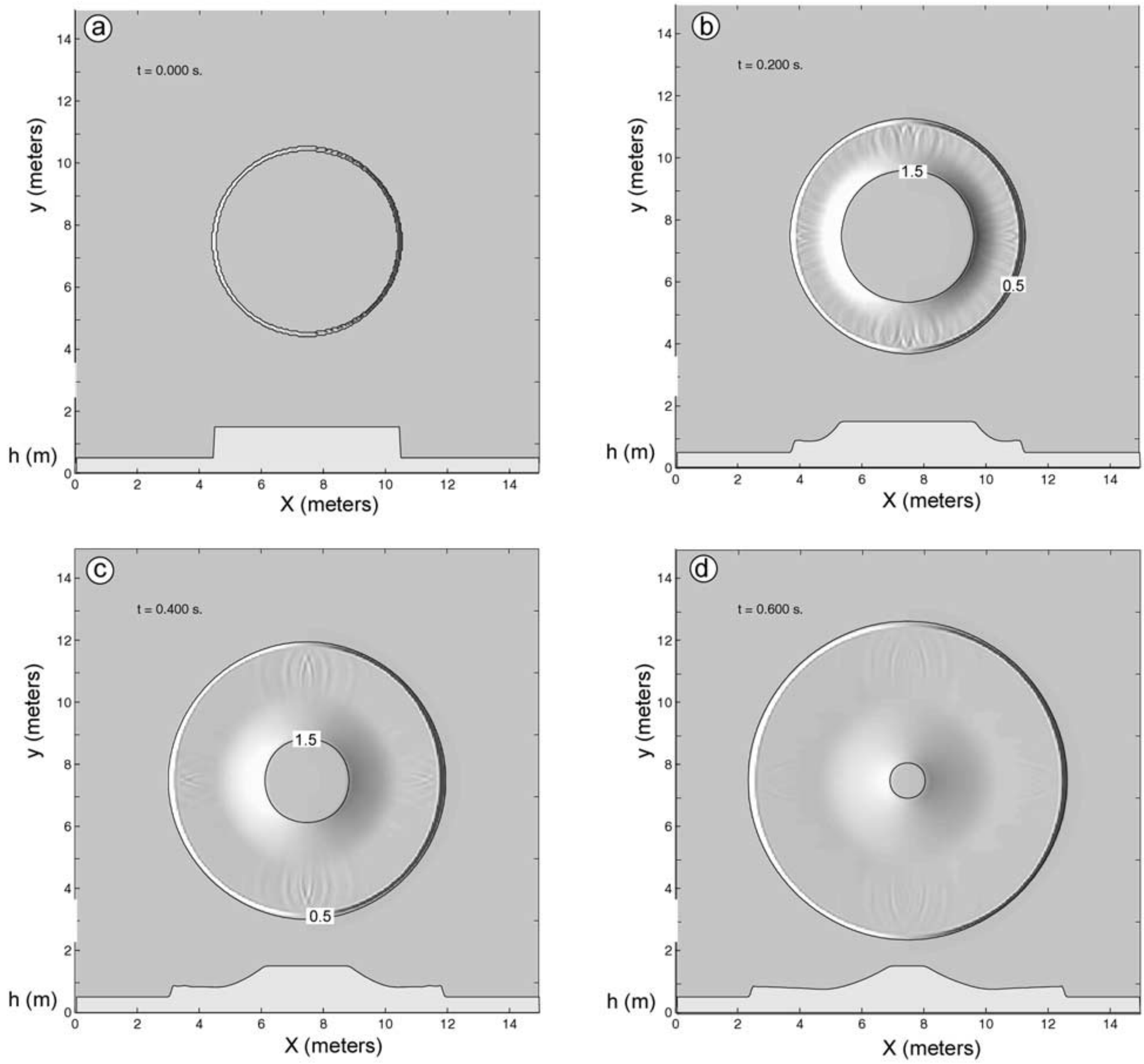

Figure 5. Circular dam break tests viewed from above (and in cross section in the lower part of each figure) show the isotropy of our numerical scheme. An initial 1.5-m-thick layer flows onto a 0.5-m-thick static layer. The surface is horizontal, and there is no friction. Parameters are dx_h = 0.05 m, dt = 0.005 s, and g = 9.81 m s^{-2}. Small numerical instabilities present in Figure 5b disappear as the flow propagates.

[15] Since our numerical scheme is based on a rectilinear coordinate system, we also performed circular dam break tests to ensure that the calculations are isotropic. In Figure 5, a 6-m-diameter cylinder of zero - friction fluid, 1.5 m thick, is released onto a 0.5-m-thick, horizontal layer of the same fluid. The resulting degree of isotropy and the shock resolution are both satisfactory, some small numerical oscillations disappearing progressively during the calculation.

[16] We also applied our code to published laboratory experiments of granular flows down chutes. These include the experiments of *Savage and Hutter* [1991], *Pouliquen and Forterre* [2002], and *Gray et al.* [2003]. In all cases our code is able to reproduce the experimental results as well as schemes presented by the authors and based on other numerical approaches (the frictional law of our model can be easily changed to take into account the various frictional laws used by the authors to reproduce their experimental results). In one numerically challenging experiment, in which a high-friction flow at high velocity encounters an obstacle [*Gray et al.*, 2003] (Figure 4), our scheme reproduces the shape and velocity of the flow; however, it is somewhat less stable than the numerical scheme used by the same authors to simulate their experiment (using the same time and space steps). The advantage of our scheme is that the computing time necessary for simulating flow over terrain with a large number of mesh cells is less than for many published methods. In this paper we calculate the emplacement of an avalanche on a 460 $\times$ 570 mesh topography in about 1 day with 3 GHz computer. The

computation time could be reduced, but we have chosen a time step 5 times lower than necessary to ensure stability.

3.3. Geological Starting Conditions

[17] The preavalanche topography north of Socompa Volcano was estimated as follows. The present-day topography of the volcano and avalanche (Figure 1a) was extracted from Shuttle Radar Topography Mission (SRTM) data. Field and borehole constraints on deposit thickness [*Wadge et al.*, 1995] were used to subtract the 25 km^3 of avalanche deposit and to obtain a best estimate of the preavalanche landscape (Figure 1c). The $\sim$11 km^3 accumulation of Toreva blocks at the northern foot of the volcano were removed, and the sectorial scar filled in using Figure 13 of *Van Wyk de Vries et al.* [2001] to reconstruct the precollapse morphology of the volcano (Figure 1c). We reconstruct the La Flexura anticline north of the volcano (LF, Figure 1a) from descriptions of *Van Wyk de Vries et al.* [2001], as well as the small preexisting relief north of La Flexura. The combination of these constraints resulted in little freedom in reconstructing the precollapse morphology. Since in this paper we only model emplacement of the (fluid) 25 km^3 avalanche, 11 km^3 of the scar fill was left in place during our calculations (to slump subsequently as Toreva blocks).

[18] One significant uncertainty is the exact geometry of the initial collapse volume. In the absence of precise evidence concerning the shape of the avalanche headwall scarp (partly buried by postavalanche products), we assume two end-member cases: (1) a wedge-shaped volume with hemicylindrical headwall scarp 5 km in radius (Figures 1c and 1d), referred to in what follows as the "deep" collapse geometry, and (2) a slab-like initial slide volume, referred to as the "shallow" geometry (see the legend of Figure 1 for details). The deep geometry appears to be most compatible with field evidence [*Van wyk de Vries et al.*, 2001] and has been used for most of the simulations. The shallow geometry is not really compatible with field evidence, but provides an alternative limiting case.

4. Numerical Results

[19] Different models were run with the aim of satisfying the following field constraints: (1) best fit to the northwestern margin, where the avalanche ran up a distal slope approximately perpendicular to the flow axis, (2) best fit to the overall outline of the avalanche deposit, including the frontal lobe, and (3) reproduction of major structures observed on the avalanche deposit, in particular the median escarpment. Only models satisfying reasonably all three constraints are taken as acceptable approximations of reality. All the results presented below were obtained by flow across numerically dry topography.

4.1. Frictional Rheology

[20] Models were run assuming a frictional avalanche rheology (equation (4)) considering three combinations of basal and internal angles of dynamic friction: (1) $\varphi_{\mathrm{bed}} \ll \varphi_{\mathrm{int}} = 30°$, the static angle of friction for dry granular debris; (2) $\varphi_{\mathrm{bed}} \neq 0°$ but $\varphi_{\mathrm{int}} = 0°$; and (3) $\varphi_{\mathrm{bed}} = \varphi_{\mathrm{int}} \neq 0°$. In each case the parameters were varied in multiple simulations. The visual best fit solutions are presented in Figure 6 using the deep collapse geometry.

[21] In the first best fit model (Figures 6a–6d), $\varphi_{\mathrm{int}} = 30°$, and a value of $\varphi_{\mathrm{bed}} = 1°$ is necessary to reach the northwestern margin of the Monturaqui Basin and to produce the observed runup. A high internal friction may be realistic for Socompa avalanche, which exhibits field evidence for rafting and progressive brittle breakup of SB material on top of a base of shearing, low-friction RIF [*Van wyk de Vries et al.*, 2001]. Bed friction angles higher than 1° result in reduced run-out, and lower ones cause excess spreading. The avalanche first accelerates away from the volcano, attaining a maximum velocity of $\sim$100 m s^{-1}, before reflecting progressively off the northwestern margins of the basin (Figures 6a–6c).

[22] In model 2 (Figures 6e–6h), $\varphi_{\mathrm{bed}} \neq 0°$ but $\varphi_{\mathrm{int}} = 0°$, so that $k_{\mathrm{actpass}} = 1$. This is not necessarily unrealistic because recent experiments show that the ratio of ground-parallel to ground-normal stress is close to unity in laboratory granular flows [*Pouliquen and Forterre*, 2002]. In the absence of internal friction, a slightly higher basal friction angle (2.5°) is now required for best fit. The evolution is close to the previous case, but here waves can be observed reflecting off the western, northern, and northeastern sides of the basin (Figure 6f).

[23] Model 3 (not shown in Figure 6), in which the basal and internal angles are assumed to be the same (best fit for $\sim$2.5°), produces a result very similar to the second model. This is because the values of k_{actpass} are very similar: 1 in model 2 and 1.0038 in model 3.

[24] All three of these frictional models reproduce only very crudely the shape of the real avalanche deposit. A major failing is that, owing to the very low basal friction, the model avalanches flow off any gradients greater than 1 to 2.5° (depending on the case). After reaching their maximum limits, the avalanches drain back into the center of the Monturaqui Basin. Consequently the model deposits each have negligible thickness along their limits of maximum extent, whereas thicknesses of up to 60 m are observed along the margins of the real avalanche [*Wadge et al.*, 1995]. The effect of topographic draining is to cause excess concentration of debris on the floor of the Monturaqui Basin. Models 2 and 3 with low internal friction generate essentially flat-topped ponds that are quite different from the real avalanche. The high angle of internal friction in model 1 permits the preservation of surface topography, but comparison with that of the real avalanche is not favorable. None of the models generate a well defined surface feature resembling the 30- to 60-m-high median escarpment. The frictional models therefore fail in reproducing some first-order morphological characteristics of the real avalanche deposit.

[25] In order to assess the effect of initial slide conditions on our results, we also ran the same models using the shallow collapse geometry (Figure 7). Using the same values of φ_{int} as in Figure 6 (30° and 0°), we find best fit values of φ_{bed} (1° and 3.5°, respectively), deposit shapes, and surface morphologies that are similar to those for the deep geometry. We conclude that the form of the resulting deposit is only weakly dependent on the geometry of the collapse volume, so that our uncertainty of the latter does

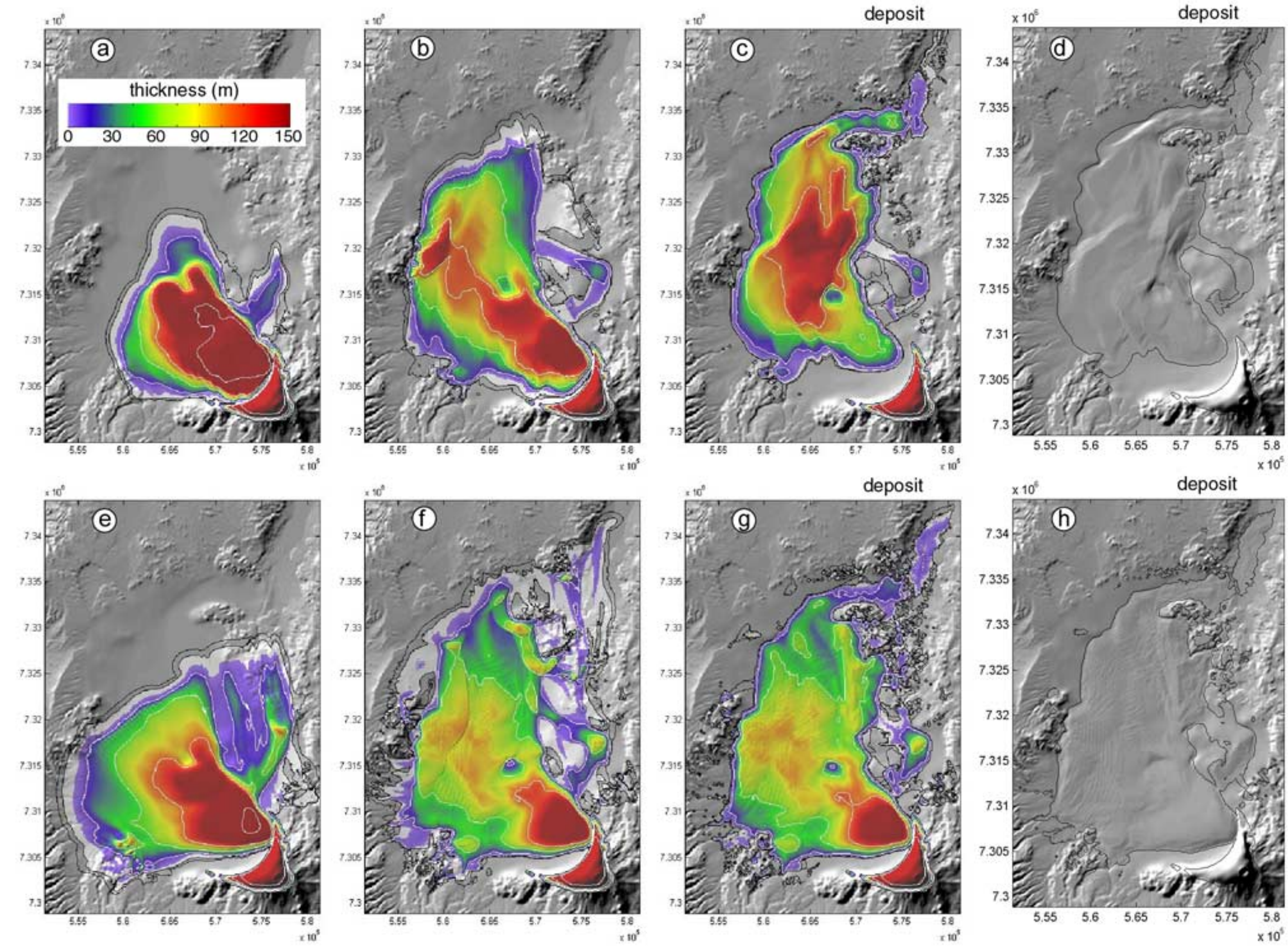

Figure 6. Snapshots of the emplacement of frictional avalanche models 1 and 2 at t = 200 s and t = 400 s, with the corresponding deposits. See text for full discussion. (a–d) Model 1, avalanche with φ_{bed} = 1° and φ_{int} = 30°. (e–h) Model 2, avalanche with φ_{bed} = 2,5° and φ_{int} = 0°. The color scale denotes the thicknesses (m) of the avalanche. Figures 6d and 6h are shaded relief maps of the final deposits. Both models assume an initial deep slide surface and vertical headwall scarp of hemicylindrical shape. Distances are given in meters (UTM).

not invalidate the apparent failure of the simple frictional models used above.

[26] We also allowed φ_{bed} to vary with the Froude number ($\| \mathbf{u} \| / \sqrt{gh}$) of the avalanche, as found for laboratory granular flows [*Pouliquen and Forterre*, 2002] and approximated [*Heinrich et al.*, 2001] by

$$\tan \varphi_{bed} = \tan \varphi_1 + (\tan \varphi_2 - \tan \varphi_1) \exp\left(-\frac{h}{D} \frac{\sqrt{gh}}{\| \mathbf{u} \|}\right) \qquad (7)$$

where φ_1 and φ_2 are limiting angles of friction (with $\varphi_2 > \varphi_1$) and D is approximately an order of magnitude larger than the mean particle size. Here, $k_{actpass}$ is considered to equal 1. Equation (6) in fact gives results comparable to model 2 ($\varphi_{bed} \neq 0°$ and φ_{int} = 0°) described above (Figures 6e–6h). The effect of velocity is to increase φ_{bed} over and above the static value (φ_1). For the mean value of φ_{bed} necessary to reproduce the observed run-out (2.5°), φ_1 needs to have an even lower value, irrespective of D and φ_2. Once a given part of the avalanche is slowing down, φ_{bed} reverts to φ_1 and, as in the constant-φ_{bed} case, formation of surface topography is prevented by the high fluidity of the material. It is worth noting that values for φ_1, φ_2 and D used by *Heinrich et al.* [2001] to simulate the ~0.005 km^3 26 December 1997 debris avalanche on Montserrat (11°, 25° and 15 m, respectively) result in a run-out for Socompa that is much smaller than that observed. Using a more complete form of equation (7) [*Pouliquen and Forterre*, 2002] gives slightly better results because the friction angle increases just as the avalanche comes to rest, allowing structures to be preserved. However, while this law gives very good results for simulated laboratory experiments, we have not found any combination of the six free parameters that give a good fit in the case of Socompa.

[27] Finally, we note that the well known Voellmy rheological law also fails to satisfy all three constraints at Socompa. The Voellmy law consists of a frictional stress plus a positive stress term proportional to velocity squared [e.g., *Evans et al.*, 2001]. Although entirely empirical, it has been widely used to model snow and rock avalanches in two dimensions. However, in the case of Socompa we find that it fails to generate realistic results for a similar reason as equation (7).

[28] In summary, simple frictional models are able to reproduce the approximate run-out of Socompa avalanche

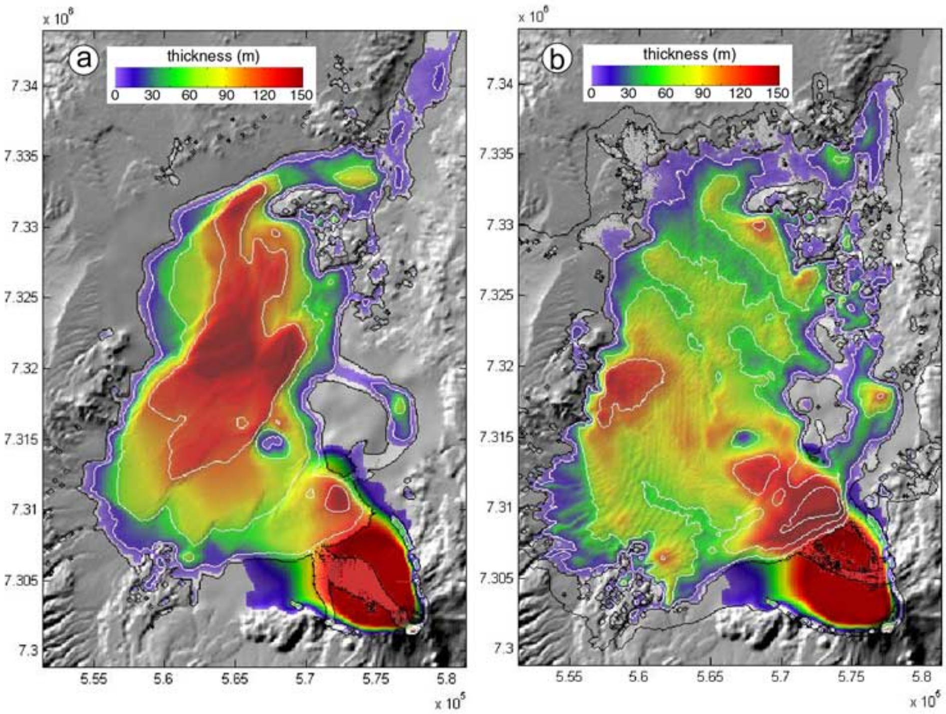

Figure 7. Best fit simulations using a shallow slab-like initial slide geometry, to be compared with the deep geometry shown in Figure 6. The color scale denotes thickness. (a) Avalanche with $\varphi_{\mathrm{int}} = 30°$. Visual best fits require approximately the same value of $\varphi_{\mathrm{bed}} = 1°$ for this shallow geometry as for a deep geometry. (b) Avalanche with $\varphi_{\mathrm{int}} = 0°$. Visual best fits require $\varphi_{\mathrm{bed}} = 3.5°$ for this shallow geometry compared with the 2.5° for the deep case in Figure 6.

only if very low values are used for the basal dynamic friction. However, they are unable to generate deposits either with realistic thicknesses on slopes greater than about three degrees, or realistic surface morphology such as the median escarpment. This is because the low basal friction angles necessary for long run-out also result in strong topographic drainback.

4.2. Constant Retarding Stress

[29] In view of the apparent inadequacy of the simple frictional models, we also ran models in which the retarding stress T in equations (2) and (3) was constant (k_{actpass} was taken as unity). This very simple assumption was motivated by the study of *Dade and Huppert* [1998], who found that the field data for a large number of avalanches can be explained by an approximately constant retarding stress.

[30] The models produce surprisingly good fits to the real avalanche provided that T lies in the range 50–100 kPa, depending on the initial slide geometry chosen. Using the deep collapse geometry the overall distribution is reproduced reasonably well with a value of 52 kPa (Figure 8), but with slight excess spreading to the west and east. A 75 kPa resistance produces realistic fits to the western and eastern boundaries, but the northwestern limit is not reached. In the case of a (geologically less realistic) shallow collapse, a resistance of 100 kPa is required, but the frontal lobe is less well produced.

[31] Unlike the frictional rheologies, this law produces a deposit with a well defined edge and leaves a deposit of realistic [*Wadge et al.*, 1995] thickness on all slopes, irrespective of angle. Surface structures on the model deposit are remarkably similar to those of the real avalanche (Figures 8d and 8e). In particular, a well-defined NE-SW trending topographic discontinuity (ME, Figure 8) strongly resembles the median escarpment, both in height (20 to 50 m) and location.

[32] Snapshots of the 52 kPa simulation (Figure 9, colored for velocity, see also Animation 1) provide an explanation for the origin of the median escarpment. The avalanche accelerates down the northern flank of the volcano, attaining a maximum speed of $\sim$100 m s^{-1}. As it runs up the western, then northwestern, slope of the basin, it reflects as three waves (one main one and two smaller ones) that then merge and wash back across the basin. The front of this composite wave then freezes to form the median escarpment. The elevated zone located north of the frozen wave front is also observed on the real avalanche deposit, and in the model represents the peak of the reflected wave (CZ, Figure 8). This area, which in the natural deposit is rich in complex fault structures, experiences a complex history during the simulation, involving (1) initial stretching as the avalanche accelerates away from the volcano (Figure 9a), (2) compression as the material decelerates and accumulates against the northwest margin (Figure 9c), and (3) stretching and shearing during reflection off the northwest margin (Figures 9d and 9e). Other similarities between the simulated and real deposits include the frontal lobe (FL, Figure 8) and the overthickened margins along the northwestern limit of the avalanche that in the model

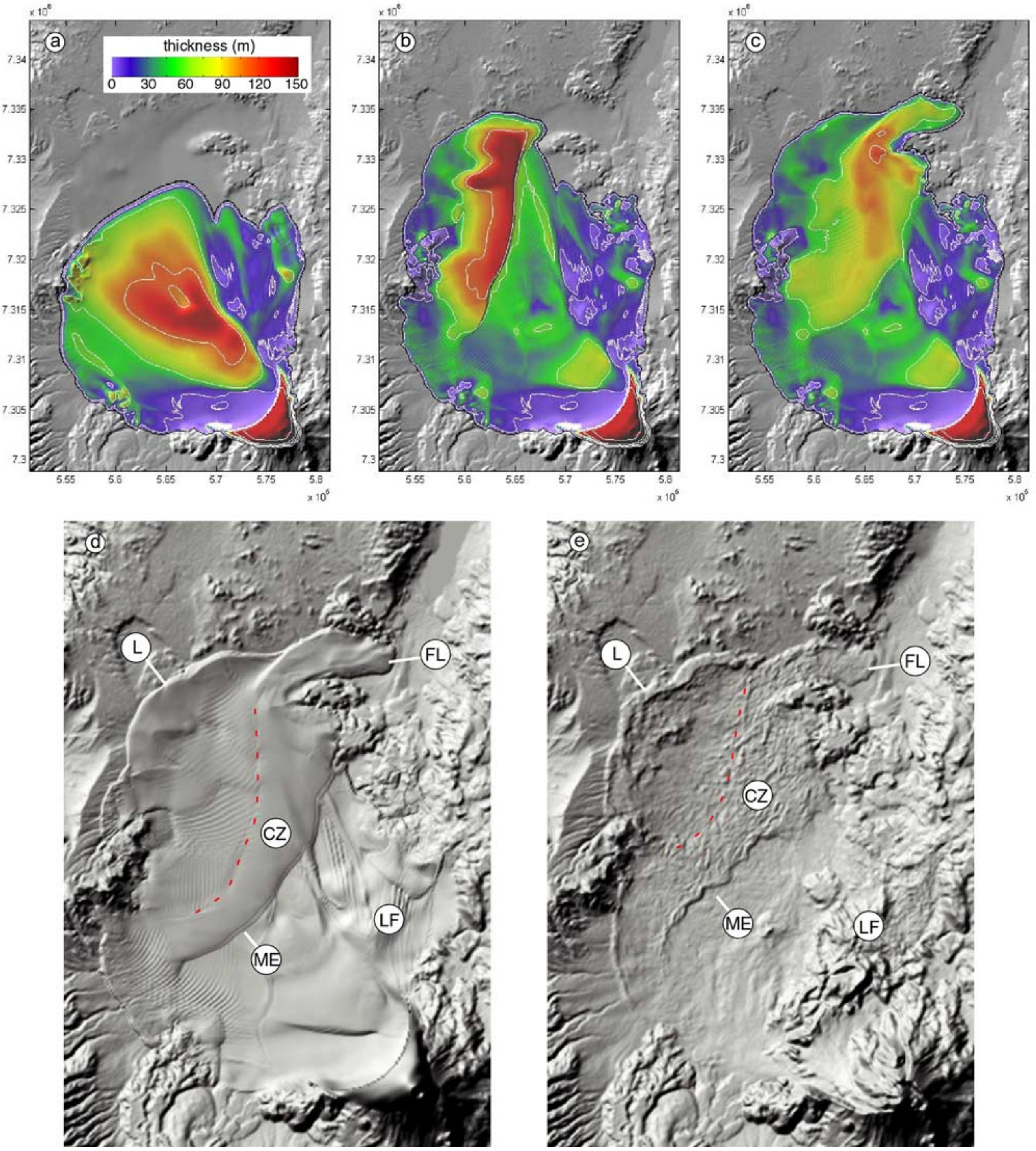

Figure 8. Avalanche evolution using a constant retarding stress T = 52 kPa. The color scale denotes thickness. The initial deep slide geometry is used in this simulation. (a–c) Snapshots at 200 s, 400 s, and 600 s. (d) Shaded relief map of the simulated deposit. (e) Shaded relief map of the real deposit.

form by accumulation, then back slumping, of material during wave reflection.

5. Discussion

[33] We have carried out numerical modeling of the emplacement of Socompa avalanche using the depth-averaged equations for granular flow and a numerical scheme capable of resolving shocks to a high degree of accuracy. The models assume transport of the avalanche on a basal slip layer, as suggested by evidence at Socompa and avalanche deposits. Starting conditions are consistent with field observations. The avalanche is assumed to have traveled as a single mass, with the exception of the Toreva blocks, which in our models are left to slump after avalanche emplacement.

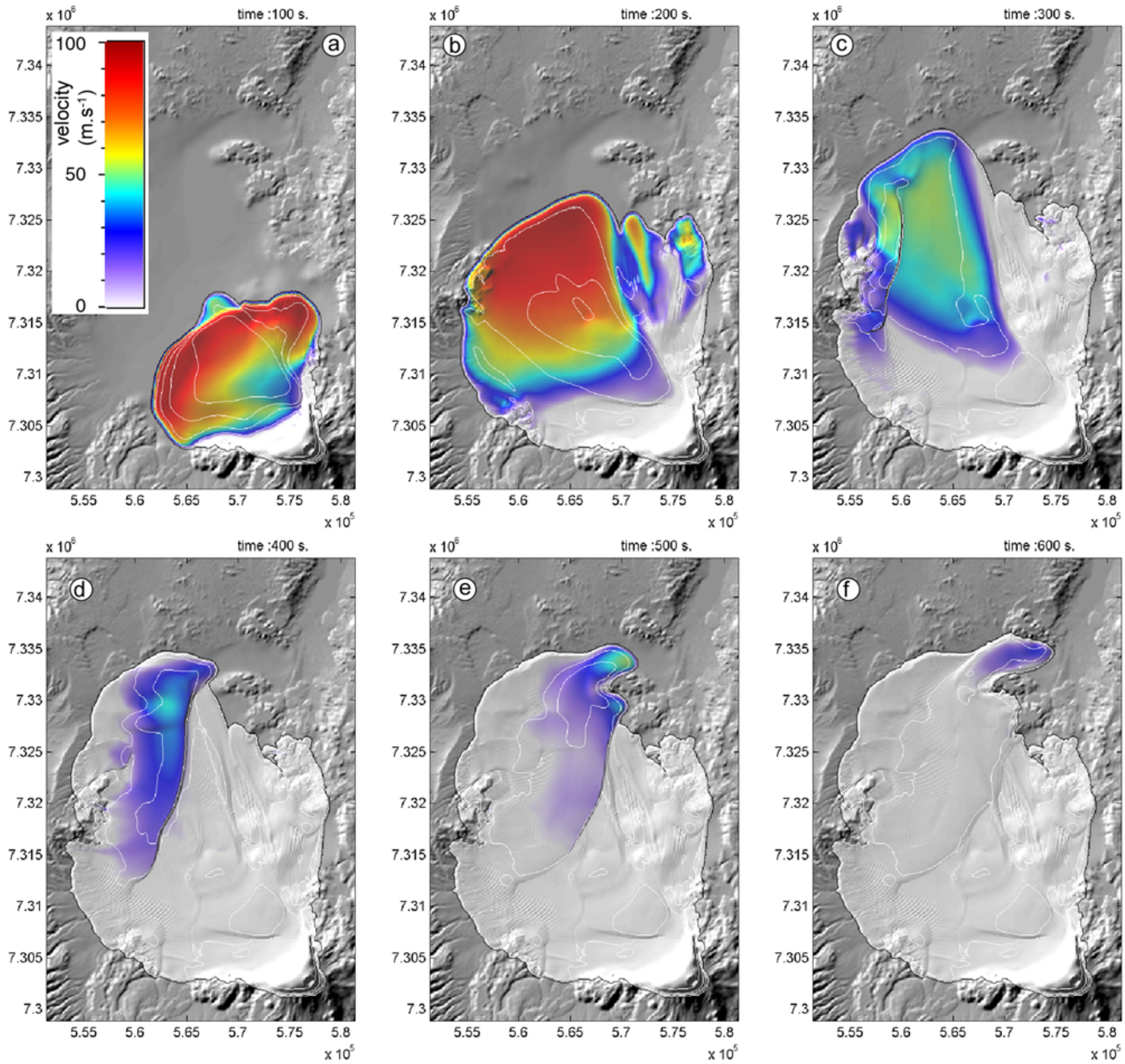

Figure 9. Snapshots every 100 s of the constant stress (52 kPa) simulation of Figure 8, colored according to velocity (m s^{-1}). The reflected wave is particularly clear in these figures, as is the late stage emplacement of the frontal lobe. See Animation 1 for video version.

[34] The high "mobility" of long run-out avalanches is normally interpreted in terms of reduced dynamic friction. The results of our modeling using frictional laws indeed confirm that very low basal friction (3° or less) is required to explain run-out at Socompa, irrespective of the internal value. This agrees approximately with the value of arctan (H/L) for the avalanche, which is 4.3° if the maximum values of H (height drop) and L (horizontal run-out) are used. Simple scaling arguments show that $(H/L) \sim \tan \phi$, where ϕ is the mean dynamic friction angle during emplacement [e.g., *Pariseau and Voight*, 1979]. The long run-out cannot be explained by gravitational spreading of a very large volume of rock debris with normal friction. Use of values of ϕ in the range 20°–30° typical of dry granular materials results in run-outs that are grossly inferior to that observed. No variation of the geometry of the initial slide mass within geologically realistic limits changes this conclusion.

[35] Many hypothetical mechanisms of friction reduction have been proposed for rock avalanches; see *Davies and McSaveney* [1999], *Legros* [2002], and *Collins and Melosh* [2003] for recent summaries. We focus here on just a few that are relatively well constrained physically. Elevated pore fluid pressure may play an important role in friction reduction in many avalanches by decreasing the effective normal stress at the bed. Fluid pressures close to lithostatic have been measured in debris flows [*Major and Iverson*, 1999] and are likely in wet rock avalanches such as Mount St. Helens [*Voight et al.*, 1983]. Although there was insufficient water in Socompa avalanche for subsequent decantation and mudflow formation, saturation of a thin

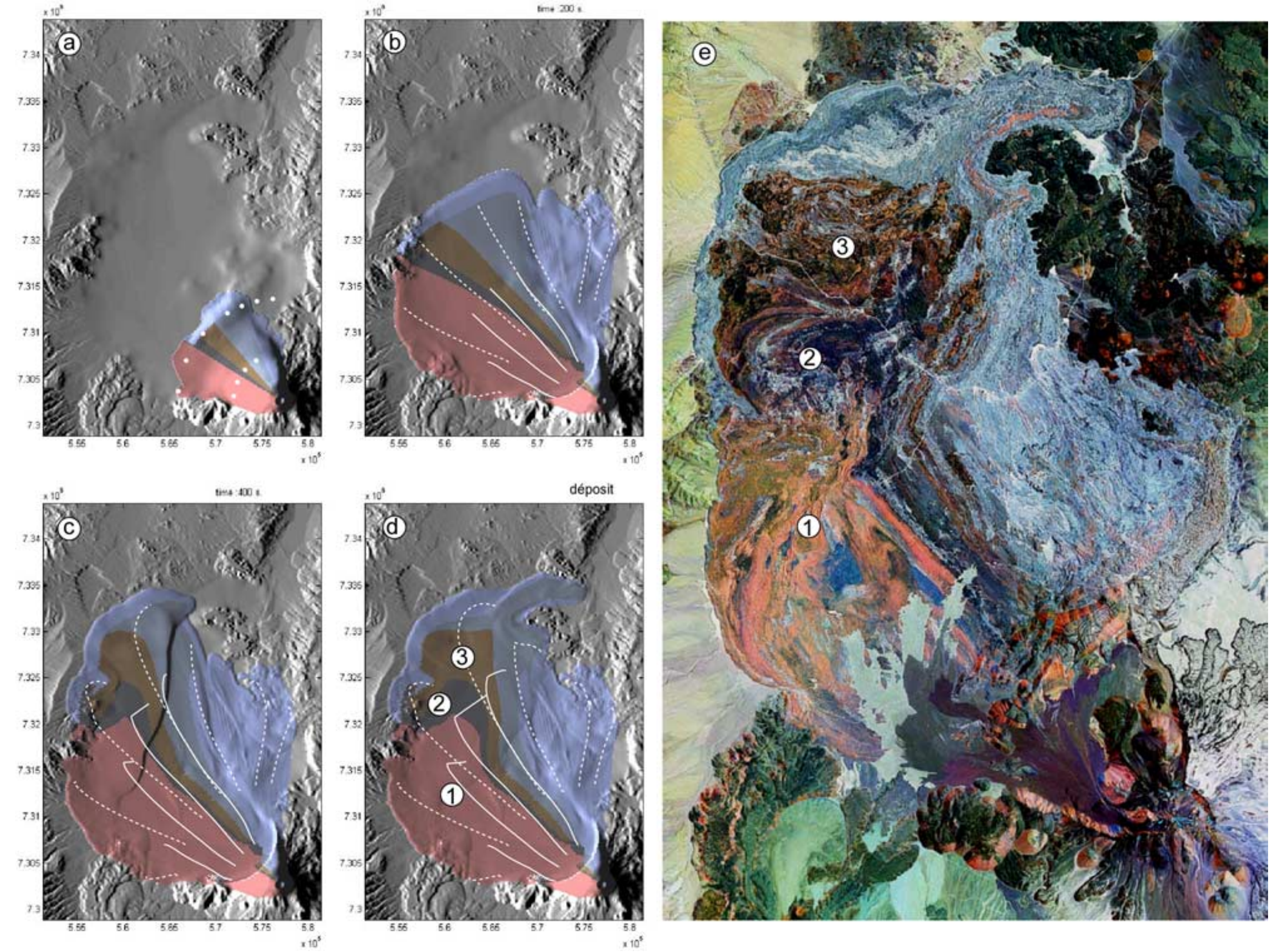

Figure 10. (a–d) Constant stress (52 kPa) simulation of Figures 8 and 9, with surface rocks colored according to lithology. Pink indicates altered Socompa lavas. Grey and brown indicate fresh lavas. Pale blue indicates ignimbrite. Ignimbrite bordering the initial avalanche front to the northeast represents the ignimbrite-cored La Flexura anticline that formed the thrust front of the initial avalanche slump. The distribution of lithology colors has been arbitrarily adjusted but is geologically realistic. White lines show the trajectories of points on the avalanche surface advected by the flow. The snapshots are at (a) $t = 200$ s, (b) 300 s, (c) 400 s and (d) the final deposit. (e) Landsat image. Numbers refer to structures visible on the simulated deposit and on the Landsat (channels 7 4 2) image.

basal layer cannot be excluded. Water could have been derived from the water table beneath the volcano or from the ground surface over which the avalanche traveled. It is possible that a shallow lake or water-saturated sediments existed in the Monturaqui Basin in late postglacial times [*Van wyk de Vries et al.*, 2001]. Pressurized hydrothermal fluids derived from the edifice and/or overridden atmospheric air could also have played a role. Other mechanisms, such as acoustic fluidization [*Melosh*, 1983; *Collins and Melosh*, 2003], mechanical fluidization [*Davies*, 1982], self-lubrication [*Campbell*, 1989; *Campbell et al.*, 1995], or dynamic fragmentation [*Davies and McSaveney*, 1999] may generate velocity dependencies of dynamic friction in the absence of pore fluids.

[36] Although frictional models can account crudely for the long run-out of Socompa avalanche, the low basal friction allows neither realistic deposition on slopes nor preservation of surface morphology like the median escarpment. A better fit is obtained if we simply assume a constant retarding stress in the range 50–100 kPa. We emphasize that we do not consider this to be necessarily an accurate rheological description of the avalanche; constraints on the starting conditions are too crude to enable any unique rheology to be inferred. Avalanches will probably exhibit very complicated time-dependent and spacially variable mechanical behavior [*Iverson and Vallance*, 2001]. Most likely, the condition represents some average value of a retarding stress that varied with time during run-out. However, it is consistent with the finding of *Dade and Huppert* [1998] that an approximately constant stress in the range 10–100 kPa can explain the spreading behavior of rock avalanches with a wide range of volumes. Indeed, it was this observation that led us to try models of this type. Other authors have also concluded that long run-out avalanches exhibit some kind of yield strength by comparing avalanche deposit thicknesses on

Earth and Mars [*McEwen*, 1989; *Shaller*, 1991]. That a constant retarding stress can also capture to a first order the emplacement dynamics of Socompa avalanche lends some support to Dade and Huppert's analysis and raises the question of the origin of this behavior.

[37] We speculate that conditions in the avalanche may have varied with time in such a way that the retarding stress could have remained approximately constant, even though the rheological behavior was fundamentally frictional (i.e., basal shear stress was a product of an apparent friction coefficient times the lithostatic normal stress, modified by a centrifugal term (equation (4)). Consider a hypothetical avalanche in which high fluid pressure is initially present in the basal shear zone, so that motion commences (when the avalanche is thick) with low basal friction. During run-out, pore fluids migrate away from the shear zone, so that friction increases progressively by pressure diffusion at the same time that the avalanche spreads and thins [e.g., *Iverson and Denlinger*, 2001]. The result could be that the basal stress remains approximately constant due to the competing effects of basal friction and flow thickness (i.e., lithostatic normal stress). In the case of a velocity-dependent process such as acoustic fluidization or mechanical fluidization, the basal friction might be reduced at initial high velocity (when the flow is thick), but would increase at lower velocities and approach the value of static friction as the avalanche comes to rest (once the flow had thinned). In both examples, acquisition of high apparent friction as avalanche motion ceased would permit preservation of surface morphology. A third possibility is that basal friction remains negligible throughout run-out (for example due to fluid pressure $\approx$ lithostatic overburden), and that the retarding stress is a cohesive component related to grinding and crushing of particles in the basal layer and/or to rock breakage within the overriding mass as it spreads across the landscape. Stresses of 50–100 kPa indeed lie in the range of cohesive strengths of volcanic materials measured in laboratory experiments [e.g., *Voight et al.*, 2002].

[38] Irrespective of the exact dynamics, our study provides two general constraints on the flow behavior of the avalanche. First, all models investigated require peak velocities of $\sim$100 m s^{-1} to achieve the observed run-out. This is due to the large height differential between the volcano summit and the basin floor (3000 m): one of the largest known for a terrestrial avalanche. Second, the results suggest that the median escarpment is the frozen front of a huge composite wave of rock debris reflected off the western, northwestern, and northern margins of the Monturaqui Basin. Reflection is observed to different extents in all the models run, but it is only in the constant-stress simulation that the wave front is preserved as a high escarpment.

[39] The reflection hypothesis is further investigated in Figures 10a–10d, in which the 52 kPa constant-stress model is rerun with the avalanche surface colored according to rock lithology. The initial distribution of lithology colors is arbitrarily adjusted, but is geologically realistic (B. Van wyk de Vries, oral communication, 2001). White tracer particles track the motion of the avalanche as they are advected along. The distribution of surface lithologies on the resulting numerical deposit closely resembles that evident on the Landsat image of the avalanche (Figure 10e). Moreover the back-reflected trails of the tracer particles mimic the stretching and folding fabrics on the avalanche surface. As the wave is reflected back in the model, material behind the wave drains northwestward to form the frontal lobe. Although certainly not a unique solution, Figure 10 demonstrates that avalanche reflection, as well as generating the median escarpment, can plausibly account for the surface textures observed on the deposit surface for a geologically realistic precollapse distribution of lithologies on and around the volcano.

[40] The topographic reflection of a huge wave of fragmented rock debris off the side of the Monturaqui Basin is a striking illustration of the high fluidity that characterizes long run-out avalanches like Socompa.

Appendix A: Numerical Scheme

[41] We use a Eulerian explicit upwind scheme where scalars (flow thickness h and ground elevation z) are defined and computed at the centers of cells, and vectors (fluxes ϕ and velocities $\mathbf{u} = (u, v)$ at the edges (Figure A1a). Mean values of flow thickness $(\overline{h})$ are computed at the edges of cells, and mean values of velocities, $\overline{\mathbf{u}} = (\overline{u}, \overline{v})$, at the centers of cells.

[42] We use cell edge $(i - 1/2, j)$ to illustrate the main steps of the algorithm (Figure A1b). For each time increment we first compute the source terms of the conservation equations, then the advection terms. The governing equations contain three source term accelerations:

$$\mathbf{a_w} = (-g \sin\theta_z \sin\alpha, -g\cos\theta_z \sin\alpha)$$
$$\mathbf{a_p} = \left(-g\ k_{\mathrm{actpass}} \cos\alpha\ dh/dx, -g\ k_{\mathrm{actpass}} \cos\alpha\ dh/dy\right)$$
$$\mathbf{a}_r = \left(-\frac{\tau}{\rho h}\frac{u}{\|\mathbf{u}\|}, -\frac{\tau}{\rho h}\frac{v}{\|\mathbf{u}\|}\right)$$

where α is the local slope, θ_z is the horizontal azimuth of that slope, and τ is the retarding stress dependant on the rheological law chosen. The algorithm first calculates a fictive velocity due just to terms $\mathbf{a}_\mathrm{w}$ and $\mathbf{a}_\mathrm{p}$. The retarding acceleration $\mathbf{a}_\mathrm{r}$ is then computed in the direction opposed to this fictive velocity. This approach increases the stability of the algorithm and ensures isotropy of the solutions. The value of new velocity (called $\mathbf{s}$) due to the action of source terms is then

$$\mathbf{s}_{i-1/2,j} = \mathbf{u}_{i-1/2,j}^{t-\mathrm{d}t} + \left(\mathbf{a}_w + \mathbf{a}_p + \mathbf{a}_r\right)\mathrm{d}t$$

[43] The second stage of the algorithm computes the advection terms. The fluxes of mass and momentum are calculated using an upwind scheme. For example, if the x component of $\mathbf{s}_{i-1/2,j}$ is negative, fluxes through the side are computed by

$$\phi_{i-1/2,j}^{h} = s_{i-1/2,j}\ h_{i,j}^{t-\mathrm{d}t}\ dy$$
$$\phi_{i-1/2,j}^{hu} = s_{i-1/2,j}\ \overline{u}_{i,j}^{t-\mathrm{d}t} h_{i,j}^{t-\mathrm{d}t}\ dy$$
$$\phi_{i-1/2,j}^{hv} = s_{i-1/2,j}\ \overline{v}_{i,j}^{t-\mathrm{d}t} h_{i,j}^{t-\mathrm{d}t}\ dy$$

Note that the superscripts of ϕ indicate the quantity advected: mass h and momentum hu and hv. From these

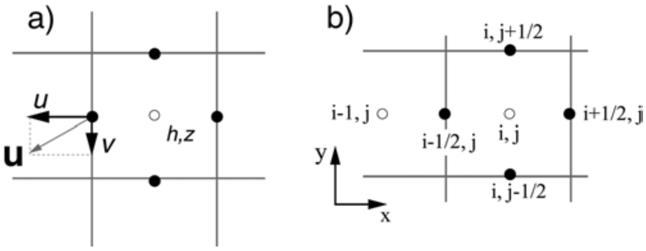

Figure A1. Definitions of (a) scalars, vectors, and (b) cell notation in the numerical scheme.

fluxes, we calculate the new thickness and the new mean velocity at the center of each cell:

$$h_{i,j}^{t} = h_{i,j}^{t-\mathrm{d}t} + \left(\phi_{i-1/2,j}^{h} - \phi_{i+1/2,j}^{h} + \phi_{i,j-1/2}^{h} - \phi_{i,j+1/2}^{h}\right)\mathrm{d}t/S$$

$$\overline{u}_{i,j}^{t} = \frac{\overline{u}_{i,j}^{t-\mathrm{d}t} h_{i,j}^{t-\mathrm{d}t} + \left(\phi_{i-1/2,j}^{hu} - \phi_{i+1/2,j}^{hu} + \phi_{i,j-1/2}^{hu} - \phi_{i,j+1/2}^{hu}\right)\mathrm{d}t/S}{h_{i,j}^{t}}$$

$$\overline{v}_{i,j}^{t} = \frac{\overline{v}_{i,j}^{t-\mathrm{d}t} h_{i,j}^{t-\mathrm{d}t} + \left(\phi_{i-1/2,j}^{hv} - \phi_{i+1/2,j}^{hv} + \phi_{i,j-1/2}^{hv} - \phi_{i,j+1/2}^{hv}\right)\mathrm{d}t/S}{h_{i,j}^{t}}$$

where S is the surface of the cell.

[44] Finally, the x and y components of the new velocities at the edges, modified by advection, are calculated using a second upwind scheme. For example, if $\overline{\mathbf{u}}_{i,j}^{t}$ and $\overline{\mathbf{u}}_{i-1,j}^{t}$ are both negative, $\overline{\mathbf{u}}_{i,j}^{t}$ will modify only the value of $\mathbf{u}_{i-1/2,j}^{t}$, and the new velocity at time t at edge ($i - 1/2$, j) is given by

$$\mathbf{u}_{i-1/2,j}^{t} = \mathbf{s}_{i-1/2,j} + \left(\overline{\mathbf{u}}_{i,j}^{t} - \overline{\mathbf{u}}_{i,j}^{t-\mathrm{d}t}\right)\frac{h_{i,j}^{t}}{\overline{h}_{i-1/2,j}^{t-\mathrm{d}t}}$$

[45] **Acknowledgments.** Ben van Wyk de Vries shared his knowledge of Socompa with us and advised us on reconstructing the preavalanche terrain. Thierry Buffard and Stephan Clain helped us test the numerical code. Barry Voight, Geoff Wadge, Herbert Huppert, and two anonymous reviewers provided useful feedback. The work was financed by two research programs of the French CNRS: "Relief de la Terre" and "Aléas et Changements Globaux."

References

Campbell, C. S. (1989), Self-lubrication for long-runout landslides, *J. Geol.*, *97*, 653–665.
Campbell, C. S., P. W. Cleary, and M. Hopkins (1995), Large-scale landslide simulations: Global deformation, velocities, and basal friction, *J. Geophys. Res.*, *100*, 8267–8283.
Collins, G. S., and H. J. Melosh (2003), Acoustic fluidization and the extraordinary mobility of sturzstroms, *J. Geophys. Res.*, *108*(B10), 2473, doi:10.1029/2003JB002465.
Dade, W. B., and H. E. Huppert (1998), Long-runout rockfalls, *Geology*, *26*, 803–806.
Davies, T. R. (1982), Spreading of rock avalanche debris by mechanical fluidization, *Rock Mech.*, *15*, 9–24.
Davies, T. R., and M. J. McSaveney (1999), Runout of dry granular avalanches, *Can. Geotech. J.*, *3*, 313–320.
Denlinger, R. P., and R. M. Iverson (2001), Flow of variably fluidized granular masses across three-dimensional terrain: 2. Numerical predictions and experimental tests, *J. Geophys. Res.*, *106*, 553–566.
Evans, S. G., O. Hungr, and J. J. Clague (2001), Dynamics of the 1984 rock avalanche and associated distal debris flow on Mount Cayley, British Columbia, Canada: Implications for landslide hazard assessment on dissected volcanoes, *Eng. Geol.*, *61*, 29–51.
Francis, P. W., M. Gardeweg, C. F. Ramirez, and D. A. Rothery (1985), Catastrophic debris avalanche deposit of Socompa volcano, northern Chile, *Geology*, *13*, 600–603.
Gray, J. M. N. T., Y.-C. Tai, and S. Noelle (2003), Shock waves, dead zones and particle-free regions in rapid granular free-surface flows, *J. Fluid Mech.*, *91*, 161–181.
Heinrich, P., G. Boudon, J. C. Komorowski, R. S. J. Sparks, R. Herd, and B. Voight (2001), Numerical simulation of the December 1997 debris avalanche in Montserrat, Lesser Antilles, *Geophys. Res. Lett.*, *28*, 2529–2532.
Iverson, R. M. (1997), The physics of debris flows, *Rev. Geophys.*, *35*(3), 245–296.
Iverson, R. M., and R. P. Denlinger (2001), Flow of variably fluidized granular masses across three-dimensional terrain: 1. Coulomb mixture theory, *J. Geophys. Res.*, *106*, 537–552.
Iverson, R. M., and J. W. Vallance (2001), New views of granular mass flows, *Geology*, *29*, 115–118.
Legros, F. (2002), The mobility of long-runout landslides, *Eng. Geol.*, *63*(3–4), 301–331.
Major, J. J., and R. M. Iverson (1999), Debris-flow deposition: Effects of pre-fluid pressure and friction concentration at flow margins, *Geol. Soc. Am. Bull.*, *111*, 1424–1434.
Mangeney, A., P. Heinrich, and R. Roche (2000), Analytical solution for testing debris avalanche numerical models, *Pure Appl. Geophys.*, *157*, 1081–1096.
McEwen, A. S. (1989), Mobility of large rock avalanches; evidence from Valles Marineris, Mars, *Geology*, *17*, 12, 1111–1114.
Melosh, H. J. (1983), Acoustic fluidization, *Am. Sci.*, *71*, 158–165.
Melosh, H. J. (1990), Giant rock avalanches, *Nature*, *348*, 483–484.
Pariseau, W. G., and B. Voight (1979), Rockslides and avalanches: Basic principles, and perspectives in the realm of civil and mining operations, in *Rockslides and Avalanches*, vol. 2, edited by B. Voight, pp. 1–92, Elsevier, New York.
Patra, A. K., et al. (2005), Parallel adaptative numerical simulation of dry avalanches over natural terrain, *J. Volcanol. Geotherm. Res.*, *139*, 1–21.
Pouliquen, O., and Y. Forterre (2002), Friction law for dense granular flows: Application to the motion of a mass down a rough inclined plane, *J. Fluid Mech.*, *453*, 133–151.
Savage, S. B., and K. Hutter (1989), The motion of a finite mass of granular material down a rough incline, *J. Fluid Mech.*, *199*, 177–215.
Savage, S. B., and K. Hutter (1991), The dynamics of avalanches of granular materials from initiation to runout. part I: Analysis, *Acta Mech.*, *86*, 201–223.
Shaller, P. J. (1991), Analysis and implications of large Martian and terrestrial landslides, Ph.D. thesis, 586 pp., Calif. Inst. of Technol., Pasadena.
Takarada, S., T. Ui, and Y. Yamamoto (1999), Depositional features and transportation mechanism of valley-filling Iwasegawa and Kaida debris avalanches, Japan, *Bull. Volcanol.*, *60*, 508–522.
Toro, E. F. (2001), *Shock-Capturing Methods for Free-Surface Shallow Flows*, 309 pp., John Wiley, Hoboken, N.J.
Van Wyk de Vries, B., S. Self, P. W. Francis, and L. Keszthelyi (2001), A gravitational spreading origin for the Socompa debris avalanche, *J. Volcanol. Geotherm. Res.*, *105*, 225–247.
Voight, B., R. Janda, H. Glicken, and P. M. Douglas (1983), Nature and mechanics of the Mount St. Helens rockslide-avalanche of 18 May 1980, *Geotechnique*, *33*, 243–273.
Voight, B., et al. (2002), The 26 December (Boxing Day) 1997 sector collapse and debris avalanche at Soufrière Hills Volcano, Montserrat, in *The Eruption of Soufrière Hills Volcano, Montserrat, From 1995 to 1999*, edited by T. H. Druitt and B. P. Kokelar, *Mem. Geol. Soc. London*, *21*, 363–407.
Wadge, G., P. W. Francis, and C. F. Ramirez (1995), The Socompa collapse and avalanche event, *J. Volcanol. Geotherm. Res.*, *66*, 309–336.

T. H. Druitt and K. Kelfoun, Laboratoire Magmas et Volcans, OPGC, UBP-CNRS-IRD, 5 rue Kessler, F-63038 Clermont-Ferrand, France. (k.kelfoun@opgc.univ-bpclermont.fr)